CMNE/CILAMCE 2007
Porto, 13-15 de Junho, 2007

NUMERICAL INVESTIGATION OF THE FLOW FIELD IN CONFINED IMPINGING JETS OF POWER LAW FLUIDS

A. S. Cavadas [1], **F. T. Pinho** [1,2] **e J. B.L.M. Campos** [3]

1 Centro de Estudos de Fenómenos de Transporte
Faculdade de Engenharia
Universidade do Porto
Rua Roberto Frias, 4200-465 Porto, Portugal
adelioc@fe.up.pt
2 Universidade do Minho
Largo do Paço, 4704-553 Braga, Portugal
fpinho@fe.up.pt, fpinho@dem.uminho.pt
3 Centro de Estudos de Fenómenos de Transporte
Departamento de Engenharia Química da Faculdade de Engenharia
Universidade do Porto
Rua Roberto Frias, 4200-465 Porto, Portugal
jmc@fe.up.pt

Keywords: Impinging jets, Newtonian fluids, shear-thinning fluids, Finite volume method

Abstract. *A numerical investigation was carried out to characterize the isothermal flow in a confined impinging jet emanating from a rectangular duct of aspect-ratio equal to 13. After impinging a flat plate the flow separated in two streams that were confined by two slopping plane walls, each making an angle of 12° relative to the plate. The fluids were Newtonian and purely viscous non-Newtonian, the latter described by a power law model. The numerical simulation was carried out with a finite-volume based code using non-orthogonal collocated grids and second order accurate differencing schemes to discretize all terms of the transport equations. The flow characteristics were studied as a function of shear-thinning intensity for Reynolds numbers between 10 and 800. Specifically, we investigate in detail the pressure loss in the cell and the size of the recirculation zone attached to the sloping surfaces of the cell after validation of the numerical simulations against experimental Newtonian and non-Newtonian data. Three dimensional effects due to the finite span of the rectangular duct and cell are also evaluated.*

1. INTRODUCTION

A numerical investigation was carried out to characterize the flow field in a confined impinging jet emanating from a rectangular duct. The jet impinges a solid surface and spreads along the plate leading to intense levels of heat and mass transfer. Therefore, impinging jets are frequently found in metal cooling processes and in food and pharmaceutical industries. Here, the objective is the investigation of the dynamics of impinging jets for Newtonian and purely viscous non-Newtonian fluids.

In this set-up, of relevance for membrane separation cells, the impinging jets are confined by sloped planned walls. The jet emanating from a rectangular duct impinges a plate and splits into two streams that flow along channels of variable cross-channel due to the slopping walls. Previously, Garimella and Rice [4] studied a similar flow in the corresponding axisymmetric condition and they divided the flow field into three different regions: the free-jet region, which is sufficiently far from the impinging surface to be affected by the plate; the impinging region, where the streamwise velocity strongly decays, and the jet spreads as it approaches the plate, and the wall region downstream the impingement. More recently, the laminar flow of a jet confined by a conical wall was investigated by Miranda et al[8] who found a recirculation zone close to the conical wall at low jet Reynolds numbers. At high jet Reynolds numbers the recirculation zone grows, the fluid flows radially in a thin channel attached to the impingement plate, and a second recirculation zone develops in the expansion region close to the plate. If the nozzle-to-plate distance increases, the second recirculation also grows.

In the present study, the duct to plate distance is very short, 20% of the duct height, and the presence of the impingement plate is felt at the duct exit.

This paper numerically investigates the combined effects of shear-thinnng and flow inertia upon the pressure loss and on the length of the separated flow region in the cell for laminar flow conditions and using a proprietary CFD code. This numerical investigation is carried out after validation against experimental data obtained by Cavadas et al.[2]. An attempt is made at understanding the various contributions to the pressure loss in the cell via a simplified one-dimensional theory and using the numerical predictions to quantify some of the terms of the theory. The next sections describe, briefly, the cell geometry and the governing equations used to perform the numerical predictions. Then, the numerical procedure and the validation of the computational results are presented. Prior to presenting the parametric investigation of the pressure loss and the length of the separated flow region, which constitutes the objective of this work, the one-dimensional simplified theory on the contributions to the pressure loss is explained. The paper ends with a summary of the main conclusions.

2. FLOW GEOMETRY AND REYNOLDS NUMBER

The cell test section is schematically represented in **Fig.** 1 (a) together with the coordinate system used in this work and a photo is shown in **Fig.** 1 (b). The test section is located downstream of a rectangular duct of aspect ratio (AR) equal to 13 (with a cross-section area of 260 x 20 mm^2). This rectangular duct is 130 channel heights (H) in length in order to fully-develop the flow prior to the impinging zone. The fully-developed rectangular duct flow exits the duct and impinges a flat plate, which is confined by two slopping plane walls, each making an angle of 12° relative to the plate. The two outgoing rectangular channels at the end of the cell have an height (*h)* of 4 mm and a spanwise dimension (*W*) of 260 mm.

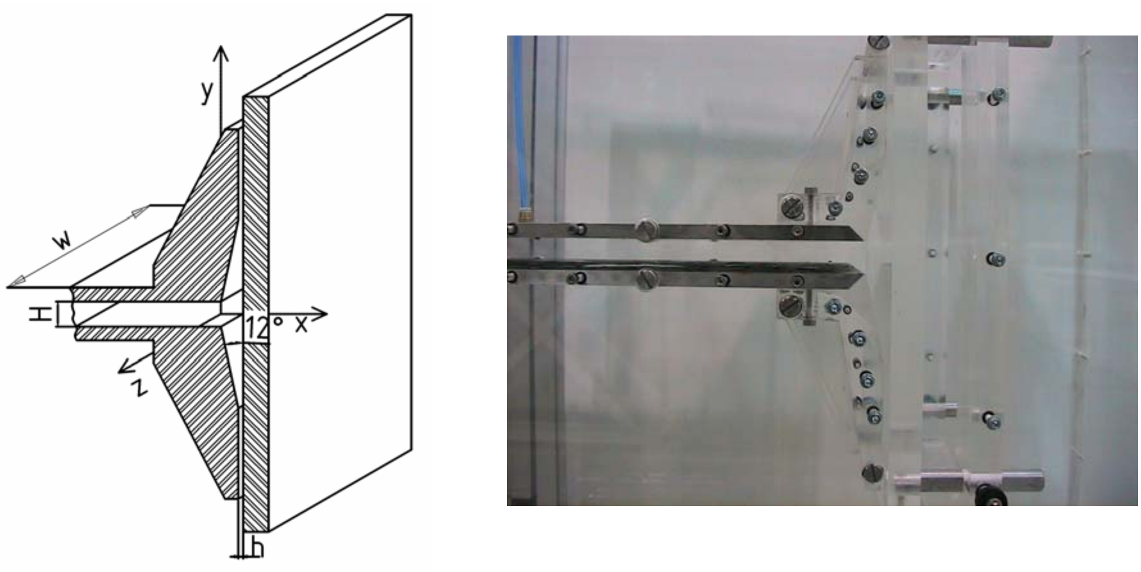

(a) (b)

Fig. 1 – Experimental set-up for the impinging jet; (a) sketch of the cell test section; (b) photo of the cell test section.

3. GOVERNING EQUATIONS

The basic equations solved are those for 3-D, incompressible and isothermal laminar flow for constant density purely viscous fluids, where the viscosity only depends on the second invariant of the strain-rate tensor (S_{ij}). In Cartesian index notation the governing equations are the continuity equation:

$$\frac{\partial u_i}{\partial x_i} = 0 \tag{1}$$

and the equation for conservation of linear momentum :

$$\frac{\partial \rho u_i}{\partial t}+\frac{\partial \rho u_j u_i}{\partial x_j}=-\frac{\partial p}{\partial x_i}+\frac{\partial \tau_{ij}}{\partial x_j} \tag{2}$$

where u_i is the velocity component along the Cartesian coordinate x_i, ρ the fluid density, p the pressure and τ_{ij} the extra stress tensor. These equations allow the determination of the velocity and pressure flow fields. A fully-implicit finite-volume method is used to solve Equations (1) - (2). The numerical code has been developed to allow the use of a number of different constitutive equations for viscoelastic and purely viscous fluids. The latter is the case in this work and the Generalized Newtonian fluid model of equation **(3)** is used, where the viscosity function is given by the power-law model (Eq. **(4)**), where the scalar shear rate ($\dot{\gamma}$) defined on the basis of the second invariant of the strain-rate tensor $\dot{\gamma} \equiv \sqrt{2S_{ij}S_{ij}}$ and $S_{ij}=1/2\left(\partial u_i/\partial x_j+\partial u_j/\partial x_i\right)$.

$$\tau_{ij}=\eta(\dot{\gamma})\left[\frac{\partial u_i}{\partial x_j}+\frac{\partial u_j}{\partial x_i}-\frac{2}{3}\frac{\partial u_k}{\partial x_k}\delta_{ij}\right] \tag{3}$$

$$\mu=K(\dot{\gamma})^{n-1} \tag{4}$$

K and *n* denote the consistency and power indices, respectively.

4. NUMERICAL PROCEDURE AND VALIDATION

The numerical method is briefly outlined below as it has been described in detail in Oliveira et al.[10]. The numerical simulations were carried out with a finite-volume method using non-orthogonal collocated grids and second order accurate differencing schemes to discretize all terms of the transport equations (Patankar [12] and Perić [13]). The main code is interfaced with a mesh generation pre-processor and adequate data post-processor, as described in Oliveira [9]. The basic differencing schemes were central differences for the diffusion terms and a high-resolution method, CUBISTA described in Alves et al [1], for the convective terms. The solution algorithm was a modified version of the SIMPLEC algorithm of van Doormal and Raithby [15] adapted for time marching as explained in Issa and Oliveira [5], where details to evaluate mass fluxes at cell faces are given.

Symmetry in terms of planes x-y and plane x-z was considered (**Fig.** 1 (a). This assumption was based on previous experimental work (Cavadas et al.[2]), and on preliminary numerical tests done to assess the adequacy of the computational domain. Therefore, the numerical domain adopted is just a “quarter” of the physical domain. On the centerline, an axisymmetric condition was assumed, and at the wall, all the velocity components were set to zero. At the inlet of the rectangular duct, the flow profile was set to uniform and the flow developed along the duct.

The computational grids were generated using patched blocks, one for the inlet of the channel, two for the cell zone, and one for the outlet of the channel. A schematic representation of the blocks used in the numerical simulations is shown in Fig. 2 (b) and details of the mesh are given in Table 1, listing the number of internal cells in the three directions (*Nx,Ny,Nz*) and the corresponding geometric expansion (or contraction) factors for mesh spacing (*fx,fy,fz*). The mesh spacing was non-uniform, with mesh points concentrated in the cell zone. The expansion factors used were carefully chosen to guarantee a smooth variation in the whole domain, in particular at the interfaces between the mesh-generating blocks. Several tests with different grids were initially performed to assess the adequate size of the discrete domain as well as the degree of grid refinement required for grid-independent results.

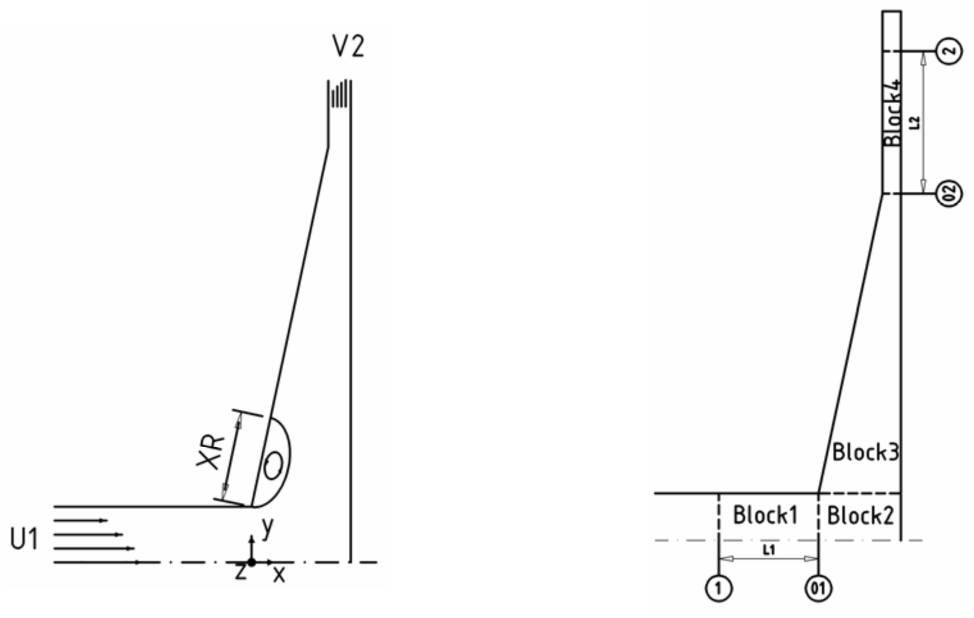

(a) (b)

Fig. 2 Schematic representation of the cell; (a) test section and measured values; (b) blocks used in the numerical simulation and tested points

Grid	Block1			Block2		
	Nx/fx	Ny/fy	Nz/fz	Nx/fx	Ny/fy	Nz/fz
M15	50/0.89258	15/1	15/1.04941	20/1	15/1	15/1.04941
M20	67/0.91831	20/1	20/1.036833	26/1	20/1	20/1.036833
M20 a)	67/0.91831	20/1	120/1.00605	26/1	20/1	120/1.00605
M30	100/0.9448	30/1	30/1.02441	39/1	30/1	30/1.02441
M30 a)	100/0.9448	30/1	60/1.012130	39/1	30/1	60/1.012130
M30 b)	100/0.9448	30/1	70/1.01039	39/1	30/1	70/1.01039
M40	133/0.9583	40/1	40/1.01825	52/1	40/1	40/1.01825

Grid	Block3			Block4			
	Nx/fx	Ny/fy	Nz/fz	Nx/fx	Ny/fy	Nz/fz	Nº total of cells
M15	20/1	88/1.00054	15/1.04941	20/1	38/1.07356	15/1.04941	53550
M20	26/1	117/1.00041	20/1.036833	26/1	50/1.05468	20/1.036833	124040
M20 a)	26/1	117/1.00041	120/1.00605	26/1	50/1.05468	120/1.00605	744240
M30	39/1	175/1.00027	30/1.02441	39/1	75/1.00027	30/1.02441	417600
M30 a)	39/1	175/1.00027	60/1.112130	39/1	75/1.00027	60/1.012130	835200
M30 b)	39/1	175/1.00027	70/1.01039	39/1	75/1.00027	70/1.01039	974400
M40	52/1	233/1.00020	40/1.01825	52/1	100/1.01825	40/1.01825	988640

Table 1 Grid dimensions;

In the grid tests, we analyze the behavior of the length (XR) of the separated regions on the sloped walls (c.f. Fig. 2(a)). This recirculation length varies along the spanwise direction and Fig. 3 shows its variation for different meshes. Grid M40 is the finest, leading to just under 4 million degrees of freedom, a large computational cost. Consequently, most simulations were carried out using grid M30 a). Even though there is a 5% difference in the length of the recirculation at the symmetry plane Z/W =0, relative to the value predicted by grid M40, the agreement with experimental data is good as shown later and hence its selection for the remaining numerical investigation. Note also that the used grid M30 a) is actually finer than grid M40 in the spanwise direction in order to better resolve variations along z.

The data in Fig. 3 pertains to a Newtonian fluid at a Reynolds number of the rectangular duct flow of 200. In this work, the Reynolds number is defined in equation (5) and follows the work of Kozicki et al [6]. It is based on the mean inlet velocity, U and on the hydraulic diameter of the rectangular channel where, for an aspect ratio of 13, the parameters a and b are a = 0.4311 and b=0.9281.

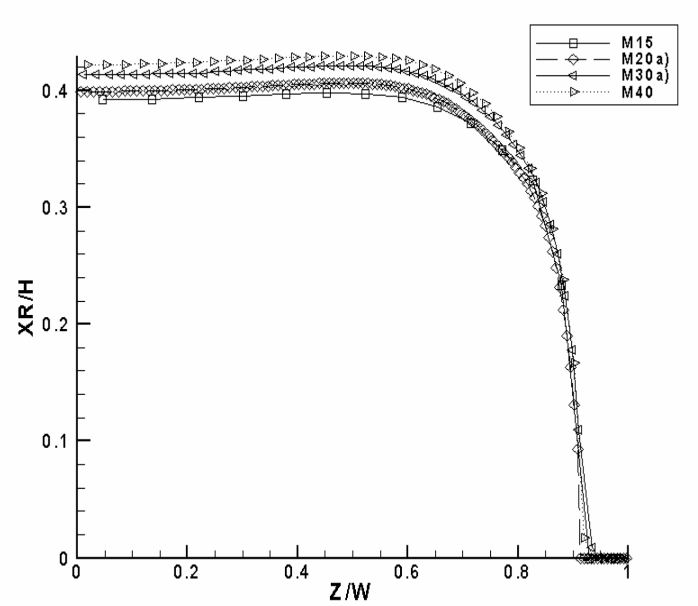

Fig. 3 Recirculation length, for $Re^*=200$, along z dimension for several mesh grids

$$Re^* = \frac{\rho (U)^{2-n} D_H^n}{8^{n-1} k \left(b + \frac{a}{n} \right)^n} \tag{5}$$

5. VALIDATION

In this Section we compare the numerical predictions with the experimental data for Newtonian and non-Newtonian fluids. For the Newtonian fluids the Reynolds numbers were $Re^*=100$ and $Re^*=200$ and for the non-Newtonian fluids $Re^*=200$. The Newtonian fluid used was a glycerol-water mixture, which had the properties listed in Table 2. The non-Newtonian fluid used was an aqueous solution of xantham-gum, at a mass concentration of 0.2%. The xantham-gum is a food-grade polymer with a high molecular weight (supplied by the Kelco Division of Merck). The viscosities were measured in a rheometer (TA-AR 2000) using a cone-plate geometry. The viscosity of the xanthan gum solution was fitted with the Carreau-Yasuda model (Eq.**(6)**), which had the rheological parameters listed in Table **(6)** .

$$\mu = \mu_\infty + (\mu_0 - \mu_\infty) \left[1 + \left(\lambda \dot{\gamma} \right)^a \right]^{\frac{n-1}{a}} \tag{6}$$

Fluid	ρ_l [kg/m^3]	μ_0 [Pa.s]	μ_∞ [Pa.s]	λ [s]	a	n	K
0.2% XG	1000	2.3242	0.00996	11.6875	0.50339	0.3454	------
Glycerol-water	1184	------	------	------	------	1	0.0425

Table 2- Rheological properties of fluids used in the experimental work at 20ºC

The validation of the numerical predictions is carried out with three sets of data:

1) Predicted transverse profiles of streamwise velocity along the rectangular duct are compared with analytical solutions for fully-developed flow and with experimental data. This comparison is aimed at ensuring that the flow is completely fully-developed well upstream the inlet of the cell.;

2) Transverse profiles of streamwise velocity within the cell;

3) Spanwise profiles of streamwise velocity within the cell.

The velocity data was normalized by the mean velocity at the rectangular channel, the *X* and *Y* coordinates by the height of the duct (H) and the *Z* coordinate by the half-width of the channel (W).

In Fig. 4 (a) the transverse profiles pertaining to the fully-developed Newtonian flow in the rectangular duct are plotted at both Reynolds numbers. The plot includes the analytical solutions for both this channel (AR=13) and an infinite channel (AR=∞), presented by White[14]. The numerical simulations obtained with grid M30 a) are in excellent agreement with the theoretical solution for the rectangular duct and differ only by 5% from the experimental data.

In Fig. 4(b) the experimental transverse profiles of the streamwise velocity at Y/H=0.8 and Z/W=0.45 are represented and compared with the results from the numerical simulation for Re^*=100 and Re^*=200 (Newtonian fluid). Here, the flow is no longer fully-developed and there is no analytical solution. As we can see there is a good agreement between the numerical and experimental data.

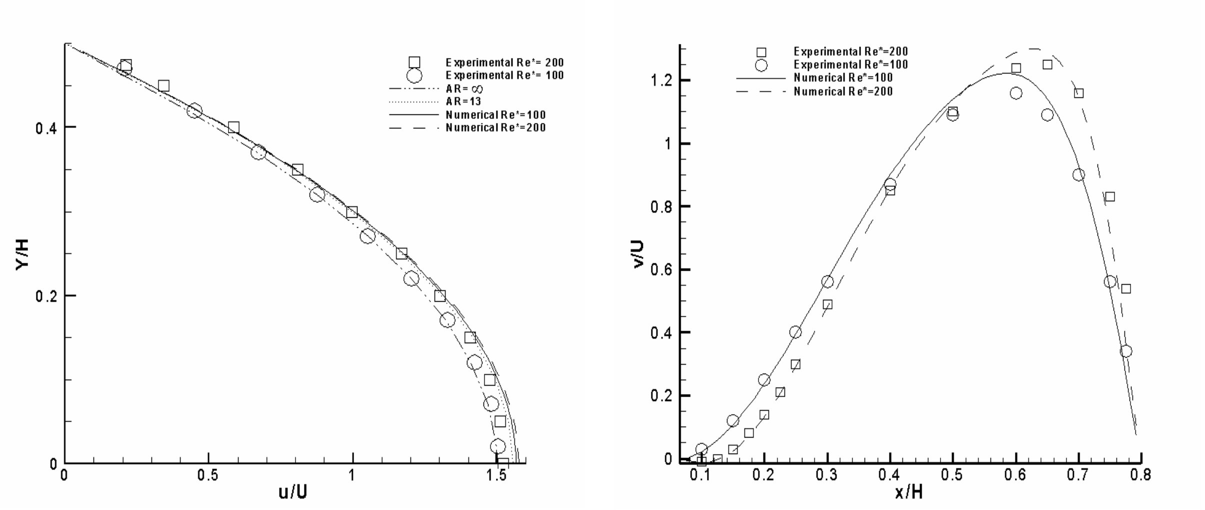

(a) (b)

Fig. 4 Comparison between experimental data (symbols), theoretical expressions and numerical simulation results for the flow of Newtonian fluids in the rectangular duct, $Re^*=100$ and $Re^*=200$; a) X/H=-5.7, Z/W=0, b) Y/H=1.65, X/H=0.525

Inside the cell, spanwise profiles of streamwise velocity at Y/H= 1.65 X/H= 0.525 (see **Fig.** 5b) for location) are represented in **Fig.** 5(a) and a good agreement is again seen between the numerical and experimental data at both Reynolds numbers, where the maximum difference is about 5%. The predicted velocity profile has the same shape as the experimental profile, with two peaks appearing near the walls, corresponding to the merging of the fluid exiting the recirculation bubble near the side walls with the main flow (this three-dimensional phenomenon will be better explained in section **7.3)**.

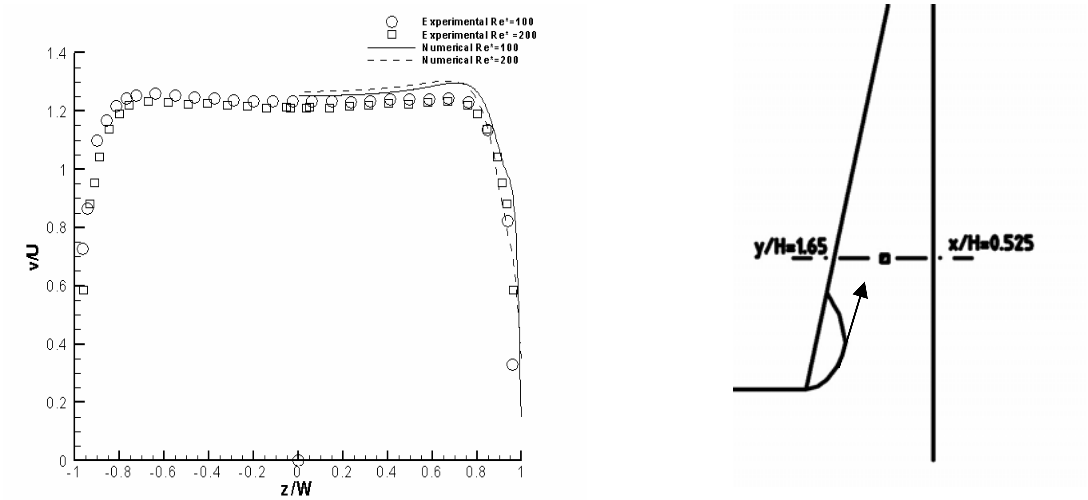

(a) (b)

Fig. 5 Spanwise profiles of streamwise velocity at the marked z-x planes within the cell for Re*=100, Re*=200

In Figures 6(a) and (b) comparisons are shown for the xanthan gum solution. In Fig. 6 (a) the profiles are in a region of fully-developed flow and the analytical solution shown pertains to $AR = \infty$. Judging from the corresponding Newtonian cases in Fig. 4 (a) the correct profile for this power law fluid in the AR=13 duct would exhibit a higher velocity on the centerline than the $AR = \infty$ case, approaching closely the calculated profile. Inside the cell, spanwise profiles of streamwise velocity at Y/H= 1.65 X/H= 0.525 (see **Fig. 5** (b) for location) are represented in Fig. 7 (a) and we can see that the predicted and measured velocity profiles have the same shape , spite of a small difference of 10%. It is interesting also to remark that the calculations were able to predict the small oscillation near the wall as seen in the experiments.

The differences between predictions and experiments are larger than for the Newtonian case, but it must be reminded that the xanthan gum solutions are viscoelastic (Escudier et al.[3]), whereas here only the viscous behavior is captured by the adopted constitutive equation. The fluid elasticity generates an imbalance of the normal stresses which will create a secondary flow in the fully-developed rectangular duct flow, leading to changes in the streamwise velocity. The secondary flow is weak and we could not measure it in the rectangular duct, but it could explain the observed differences in the shape of the streamwise velocity profile. A better prediction will need to be carried out in the future using an adequate constitutive equation to model the elastic properties of this solution.

In spite of this limitation, the effects of inertia and shear-thinning on pressure loss and recirculation length are investigated next.

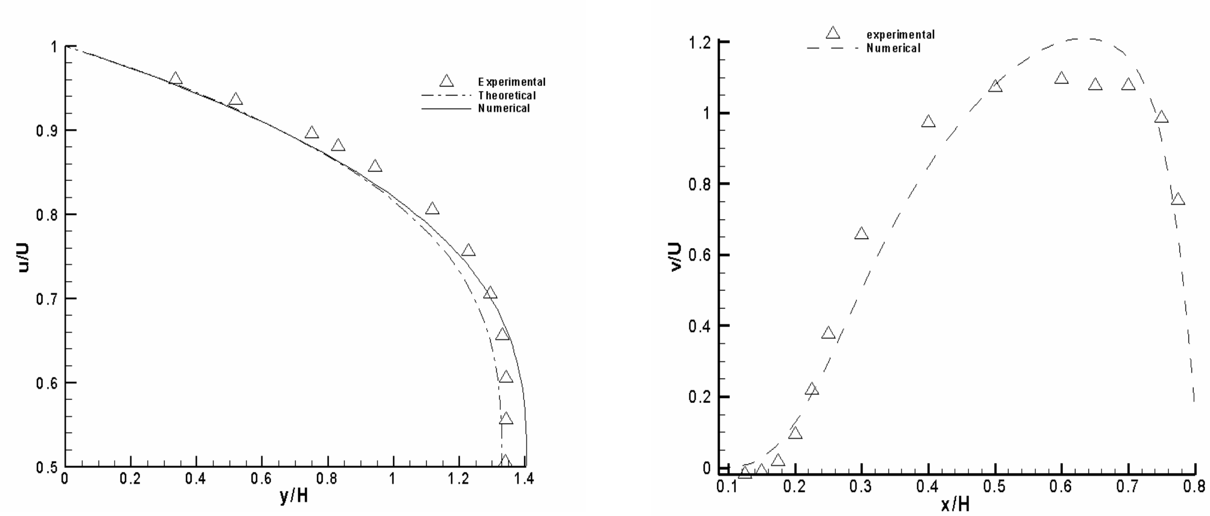

a) b)

Fig. 6– Comparison between experimental data (symbols), theoretical expressions and numerical simulation results for the rectangular duct, xanthan gum at Re*=200; (a) at X/H=-5.7 (b) at Y/H=1.65, X/H=0.525

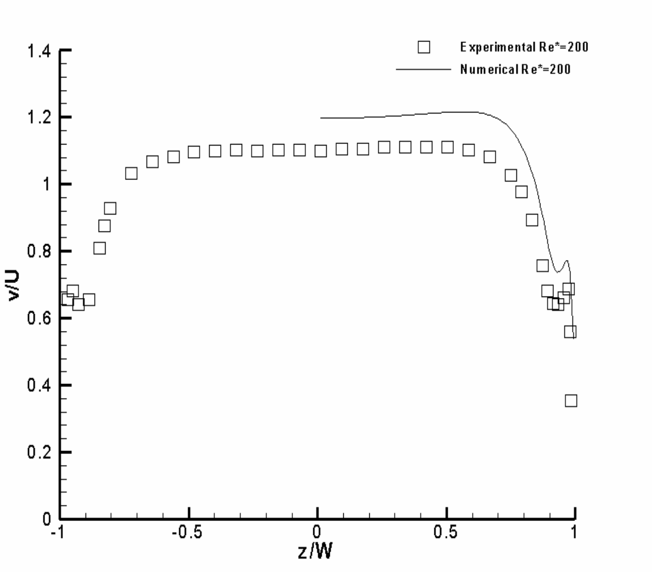

Fig. 7 Spanwise profiles of streamwise velocity at X/H=0.525, Y/H=1.65 with xantham gum at Re*=200

6. SIMPLIFIED ONE-DIMENSIONAL THEORY FOR PRESSURE LOSS

The numerical calculations allows us to directly determine the pressure loss within the cell, but it can also provide insight onto its causes, namely on the various contributions to the total pressure loss, such as the amount due to friction at the walls, inefficient flow decelerations and pressure non-uniformities, amongst others. For this purpose, prior to presenting results, a one-dimensional simplified theory, adapted from that of Oliveira and Pinho [11] for sudden expansions in pipe flow, is presented below.

In pressure drop calculations, it is engineering practice to consider that the flow is fully developed in straight pipes and ducts and to account for distortions and local effects due to fittings, curves and pipe accessories via their respective local loss coefficients. Hence, the pressure difference between sections 1 and 2 of the cell (c.f. Fig. 2 (b)) has several contributions:

- reversible increase of pressure due to the decrease of velocity along the cell (Δp_R - Bernoulli effect);
- irreversible pressure loss (Δp_I) between sections 01 and 02, that includes the inefficient dissipation of kinetic energy as the flow velocity along the cell decreases, the losses associated with the recirculation region and the pressure loss due to friction of the fluid at the walls of the cell;
- irreversible pressure loss at the inlet (between sections 1 and 01) and outlet ducts (between sections 02 and 2) (Δp_F) where the flow is mostly not fully-developed.

$$\Delta p_T = p_2 - p_1 = \Delta p_R - \Delta p_I - \Delta p_F \tag{7}$$

After normalization with the upstream dynamic pressure ($\frac{1}{2}\rho\overline{u}_1^2$), the previous equation becomes:

$$C_T = \frac{p_2 - p_1}{\frac{1}{2}\rho\overline{u}_1^2} = C_R - C_F - C_I \tag{8}$$

or

$$C_I = C_R - C_T - C_F \tag{9}$$

where C represents the corresponding pressure loss coefficient.

Assuming fully developed flow at planes 1 and 2, the integral conservation of linear momentum applied to the control volumes between 1 and 01, and between 02 and 2 (see Fig. 2 (b)) can be expressed as:

x direction:
$$p_1 A_1 + \rho A_1 \beta_1 \overline{u}_1^2 = \overline{p_{01}} A_1 + \rho A_{01} \beta_{01} \overline{u}_{01}^2 + \int \tau_{01-1}.dS_1 \tag{10}$$

y direction:
$$\overline{p_{02}} A_2 + \rho A_2 \beta_{02} \overline{v}_{02}^2 = p_2 A_2 + \rho A_2 \beta_2 \overline{v}_2^2 + \int \tau_{02-2}.dS_2 \tag{11}$$

where $\beta \equiv u^2/\overline{u}^2$ is the profile shape factor for momentum (White [14]), τ_{01-1}, τ_{02-2} are the local wall shear stresses between planes 1 and 01 and planes 02 and 2, respectively A_1 and A_2 are the cross section areas of the ducts at sections 1 and 2, respectively. The integrals can be evaluated by using average values:

$$\int \tau_{01-1}.dS_1 = \overline{\tau_{01-1}}.S_1 = \Delta p'_{F1}.A_1 \tag{12}$$

$$\int \tau_{02-2}.dS_2 = \overline{\tau_{02-2}}.S_2 = \Delta p'_{F2}.A_2 \tag{13}$$

where S_1 and S_2 are the wall surface areas where the averaged shear stresses $\overline{\tau_{01-1}}$ and $\overline{\tau_{02-2}}$ take effect.

Defining the area ratio, $\sigma \equiv A_1/A_2$, and from mass conservation $A_1\overline{u}_1 = A_2\overline{v}_2$, the combination of the above momentum balances as (Eq.(10)+ σ Eq.(11)) leads to the following expression after division by A_1 and the upstream kinetic energy.

$$C_T = \frac{p_2 - p_1}{\frac{1}{2}\rho \overline{u}_1^2} = 2(\beta_1 - \beta_{01}) - 2\sigma^2(\beta_2 - \beta_{02}) - \frac{\Delta p'_{F2} + \Delta p'_{F1} + (\overline{p_{01}} - \overline{p_{02}})}{\frac{1}{2}\rho \overline{u}_1^2} \tag{14}$$

The wall friction coefficients , C'_{F1} and C'_{F2} , and the area-averaged pressure coefficients, $\overline{C_{p01}}$ and $\overline{C_{p02}}$, are defined by:

$$C'_{F1} = \frac{\Delta p'_{F1}}{\frac{1}{2}\rho \overline{u}_1^2} = \frac{4L_1}{D_{h1}} \frac{\overline{\tau}_{w1}}{\frac{1}{2}\rho \overline{u}_1^2} \qquad C'_{F2} = \frac{\Delta p'_{F2}}{\frac{1}{2}\rho \overline{u}_1^2} = \frac{4L_2}{D_{h2}} \frac{\overline{\tau}_{w2}}{\frac{1}{2}\rho \overline{u}_1^2} \tag{15}$$

$$\overline{C_{p01}} = \frac{\overline{p_{01}}}{\frac{1}{2}\rho \overline{u}_1^2} \qquad \overline{C_{p02}} = \frac{\overline{p_{02}}}{\frac{1}{2}\rho \overline{u}_1^2} \tag{16}$$

After substitution in equation.(14) the total pressure loss coefficient is given by:

$$C_T = 2(\beta_1 - \beta_{01}) - 2\sigma^2(\beta_2 - \beta_{02}) - (C'_{F_2} + C'_{F_1} + \overline{C_{p01}} - \overline{C_{p02}}) \tag{17}$$

The reversible pressure coefficient is obtained from Bernoulli equation

$$C_R = \alpha_1 - \alpha_2\sigma^2 \tag{18}$$

where $\alpha \equiv u^3 / \overline{u}^3$ is the profile shape factor for energy.

The irreversible loss coefficient C_{IC} is now obtained combining equations (8), (14), (15) and (16).

$$C_{IC} = \alpha_1 - \alpha_2\sigma^2 - C_F - 2(\beta_1 - \beta_{01}) + 2\sigma^2(\beta_2 - \beta_{02}) + C'_{F2} + C'_{F1} + \overline{C_{p01}} - \overline{C_{p02}}\ , \tag{19}$$

an expression that can be re-written in the form of a sum of corrections to the reversible pressure coefficient

$$C_{IC} = C_R - (\Delta C_F + \Delta C_\beta - \Delta C_{p0}) \tag{20}$$

In equation (20), ΔC_β accounts for the differences in the distribution of momentum at the two inlet duct sections (1 and 01) plus the corresponding difference for the two outlet duct sections (02 and 2) ($\Delta C_\beta = \Delta C_{\beta 1} + \Delta C_{\beta 2}$), ΔC_{p0} quantifies the effects of non-uniform pressure at the inlet and outlet sections of the cell ($\Delta C_{p0} = \left(\overline{C_{p01}} - \overline{C_{p02}}\right)$) and ΔC_F represents the difference between the fully-developed (C_F) and true (C_F') pressure coefficients associated with wall friction at the inlet duct test section (1 and 01) in addition to that for the outlet duct test section (2 and 02), according to:

$$\Delta C_F = \Delta C_{F1} + \Delta C_{F2} \tag{21}$$

with

$$\Delta C_{F1} = C_{F1} - C_{F1}' \qquad \Delta C_{F2} = C_{F2} - C_{F2}' \tag{22}$$

Note that the fully developed friction coefficients are defined by:

$$C_{F1} = \frac{\Delta p_{F1}}{\frac{1}{2}\rho \bar{u}_1^2} = \frac{f_1 \frac{L_1}{D_{h1}} \frac{\bar{u}_1^2}{2} \rho}{\frac{1}{2}\rho \bar{u}_1^2} = f_1 \frac{L_1}{D_{h1}} \qquad C_{F2} = \frac{\Delta p_{F2}}{\frac{1}{2}\rho \bar{u}_1^2} = \frac{f_2 \frac{L_2}{D_{h2}} \frac{\bar{v}_2^2}{2} \rho}{\frac{1}{2}\rho \bar{u}_1^2} = \sigma^2 f_2 \frac{L_2}{D_{h2}} \tag{23}$$

The correction factors β_{0i} and $\overline{C_{p0i}}$ are calculated by numerical integration of the velocity and pressure profiles, obtained from the numerical simulations, at the plane *0i* (*i*=1,2). The values of the profiles shape factor for energy, α, and momentum, β, used in the equations above at sections 1 and 2 are presented in the Table 3.

n	α_1	α_2	β_1	β_2
1	1.63	1.55	1.22	0.48
0.8	1.58	1.49	1.21	0.47
0.6	1.51	1.43	1.19	0.46
0.4	1.44	1.34	1.16	0.45
0.2	1.32	1.23	1.12	0.43

Table 3 Values of the profiles shape for energy and momentum in sections 1 and 2

7. RESULTS AND DISCUSSION

7.1 Pressure Loss Coefficient

The values of the pressure loss coefficient C_{IC} are plotted in Fig. 8 as a function of Kozicki Reynolds number and shear-thinning intensity. The pressure loss coefficient obtained from the one-dimensional theory C_{IC} is the result of equation (19) where its various contributions were obtained from post-processing the data of the simulation with mesh

M30a).

Using the Kozicki Reynolds number, a linear dependence of both C_I and C_{IC} with the Reynolds number is seen for each value of n, especially for Re^*<400 and $n \geq 0.6$ in Fig. 8 (a). The plot also shows a reduction in C_{IC} with shear-thinning.

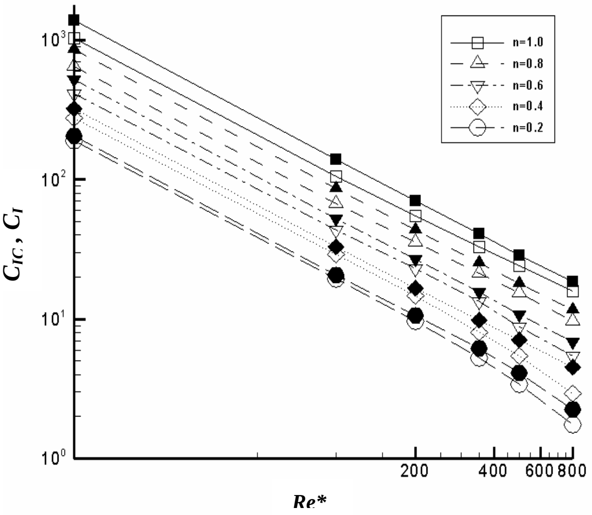

Fig. 8 C_{IC} and C_I versus Reynolds number for different values of n, filled symbols correspond to the predicted loss coefficient (C_I), open symbols to the values from the 1D theory (C_{IC}).

Using the results of the numerical simulation, each corrective term of equation (20) (ΔC_F, ΔC_β, ΔC_R and ΔC_p) can be quantified in an attempt to explain the various contributions to C_{IC}.

Differences between fully developed and undeveloped flow at the inlet (ΔC_{F1}) and outlet (ΔC_{F2}) rectangular ducts are represented in Fig. 9(a) for the case of n=1. The flow is dominated by inertia effects so the contribution of ΔC_{F1} is small at the low Reynolds numbers of this investigation and decreases to negligible values as the Reynolds number increases. The main contribution to the total friction correction comes from ΔC_{F2}, in particular at low Reynolds numbers, because the flow in the initial part of the exit rectangular duct differs from a state of fully-developed flow thus. Thus ΔC_{F2} is never negligible and, as shown below, this term is the major correction term in equation (20).

The correction due to a non-uniform pressure distribution at the inlet and outlet sections of the cell, ΔC_{p0}, is plotted in Fig. 9(b) and is seen to be relevant at low Reynolds numbers, only. The contributions to ΔC_{p0} from the inlet and outlet ducts are similar.

Figure Fig. 10(a) plots all the contributions to the pressure loss coefficient and in Fig. 10 (b) a zoom of Fig. 10 (a) is shown. At all Reynolds numbers, the most relevant contribution comes from ΔC_F whereas the effect of ΔC_β is clearly negligible. Finally, the reversible term C_R is constant and can be considered negligible at low Reynolds, but becomes important as all the corrective contributions decrease with Reynolds numbers.

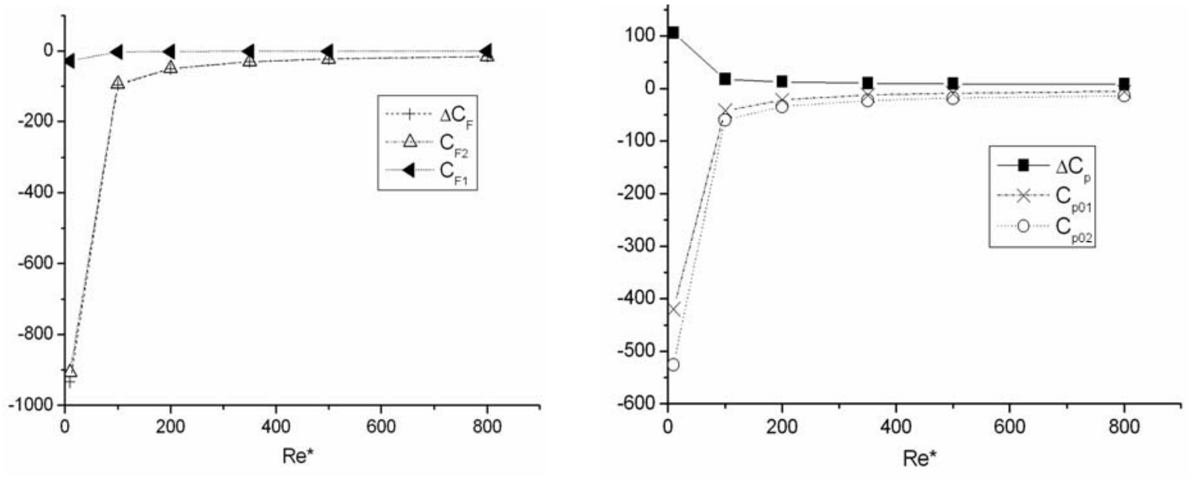

(a) (b)

Fig. 9 (a) ΔC_F, ΔC_{F1}, and ΔC_{F2} values versus Reynolds number (*n*=1); (b) ΔC_p, ΔC_{p01} and ΔC_{p02} values versus Reynolds number (*n*=1).

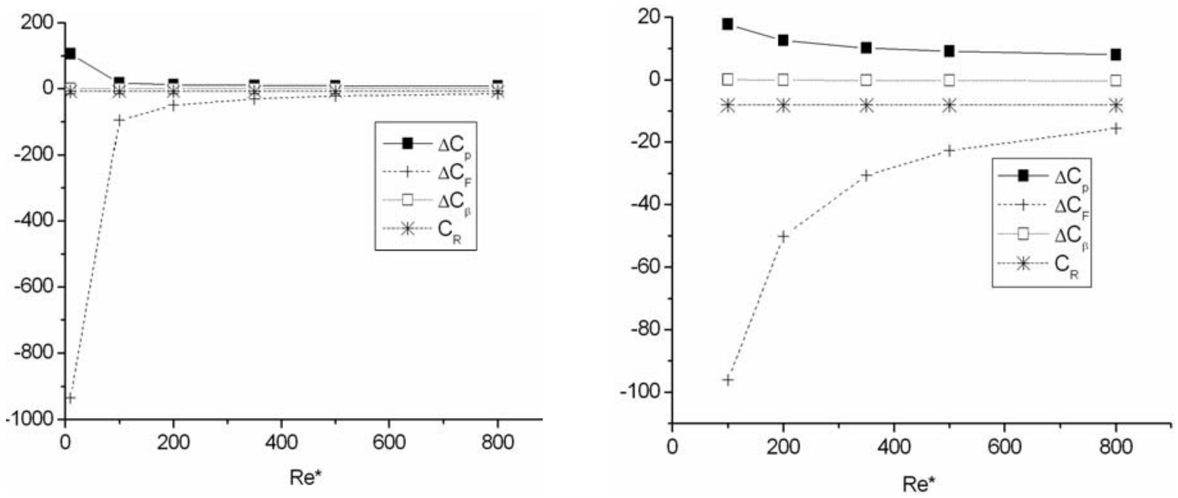

(a) (b)

Fig. 10 (a) ΔC_F, ΔC_p, ΔC_β and C_R versus Reynolds number (*n*=1); (b) zoom of ΔC_F ΔC_p, ΔC_β and C_R versus Reynolds number (*n*=1)

The correct irreversible coefficient (C_I) is determined from the variation of pressure obtained in the numerical solution of the full Navier-Stokes equations, as follows: the energy equation between planes 1 and 2, considered in area of developed flow field, (see Fig. 2 (b) reads as

$$p_1 + \frac{1}{2}\rho\alpha_1\bar{u}_1^2 + \rho g z_1 = p_2 + \frac{1}{2}\rho\alpha_2\bar{v}_2^2 + \rho g z_2 + \Delta p_{F1} + \Delta p_{F2} + \frac{1}{2}\rho C_I \bar{u}_1^2 \tag{24}$$

After simplification we obtain the following extrapolated pressures at planes 01 and 02, respectively by fitting to pressure variations only along the fully-developed regions upstream and downstream of the sloped wall: $\overline{\overline{P}}_{01} \equiv p_1 - f_1 \frac{L_1}{D_{h1}} \rho \frac{\bar{u}_1^2}{2}$ and $\overline{\overline{P}}_{02} \equiv p_2 - f_2 \frac{L_2}{D_{h2}} \rho \frac{\bar{v}_2^2}{2}$. Then, C_I is calculated using equation (25).

$$C_I = \frac{\overline{\overline{p}}_{01} - \overline{\overline{p}}_{02}}{\frac{1}{2}\rho\bar{u}_1^2} + \alpha_1 - \alpha_2\sigma^2 = \left(\overline{\overline{C}}_{p01} - \overline{\overline{C}}_{p02}\right) + \alpha_1 - \alpha_2\sigma^2 \tag{25}$$

with $\overline{\overline{C}}_{p01}$ and $\overline{\overline{C}}_{p02}$ representing the pressure coefficients just upstream and just downstream of the cell, respectively.

n=1.0						
Re*	**10**	**100**	**200**	**350**	**500**	**800**
C_{IC}	1031.8655	105.6917	54.7803	32.9200	24.0147	15.8711
C_I	1393.9001	139.9126	70.3566	40.5995	28.7335	18.4278
$(C_I - C_{IC})/C_{IC}$	26%	24.5%	22.1%	18.9%	16.4%	13.9%
n=0.8						
Re*	**10**	**100**	**200**	**350**	**500**	**800**
C_{IC}	649.3713	67.5249	35.3268	21.1972	15.3269	9.7164
C_I	852.1218	85.7277	43.2477	25.1082	17.9132	11.6629
$(C_I - C_{IC})/C_{IC}$	23.8%	21.2%	18.3%	15.6%	14.4%	16.7%
n=0.6						
Re*	**10**	**100**	**200**	**350**	**500**	**800**
C_{IC}	415.9191	43.7754	23.0167	13.3282	8.3786	5.4450
C_I	523.5901	52.7798	26.9500	15.6266	10.2057	6.9031
$(C_I - C_{IC})/C_{IC}$	20.6%	17.1%	14.6%	14.7%	14.2%	21.1%
N=0.4						
Re*	**10**	**100**	**200**	**350**	**500**	**800**
C_{IC}	273.8568	28.8660	14.7084	8.0409	5.4448	2..9376
C_I	324.6630	32.8601	16.7227	9.8744	7.0763	4.4917
$(C_I - C_{IC})/C_{IC}$	15.6%	12.2%	12.0%	18.6%	23.1%	34.6%
N=0.2						
Re*	**10**	**100**	**200**	**350**	**500**	**800**
C_{IC}	189.0694	19.4643	9.6716	5.2431	3.3948	1.7389
C_I	205.5900	20.7949	10.5827	6.1822	4.1011	2..2522
$(C_I - C_{IC})/C_{IC}$	8.0%	6.4%	8.6%	15.2%	17.2%	22.8%

Table 4 Predicted and corrected loss coefficient

Finally, we list in Table 4 all the calculated values of C_I and C_{IC} as a function of Re* and the comparison between both is plotted in Fig. 8, which constitute one of the main deliverable of this work. . At almost all Reynolds numbers there is a difference between of the predicted and the corrected of about 18%. This difference is due to the fact that we are studying a three dimensional flow and in the future should be necessary increase the number of cells along the spanwise direction.

7.2 Recirculation length

In this section we present the variation of the recirculation bubble length with Reynolds number, the shear-thinning intensity and assess for the first time some three-dimensional effects as we characterize its spanwise variation.

Figure Fig. 11 (a) plots the recirculation length (XR) along the spanwise direction (Z/W) for Newtonian fluids, as a function of Reynolds number. *XR* is constant over most of the span, with the presence of the side walls eliminating the separated flow region. The width of this central region of constant recirculation is actually decreasing with Reynolds number suggesting the strong coupling between 3D effects and inertia: for *Re*= 100 the central region occupies 70% of the channel span, decreasing to 50% at *Re*= 800. It is interesting to notice also that the longest value of XR is not at the centre plane but at the end of region where the 3D effects are detected. This effect is small, but is noticeable especially at the larger Reynolds numbers.

For the non-Newtonian fluids the picture is rather more complicated due to the combined effects of inertia, side walls and shear-thinning. For a constant Kozicki Reynolds number of 200, Fig. 11b) plots the spanwise variation of XR for different values of n.

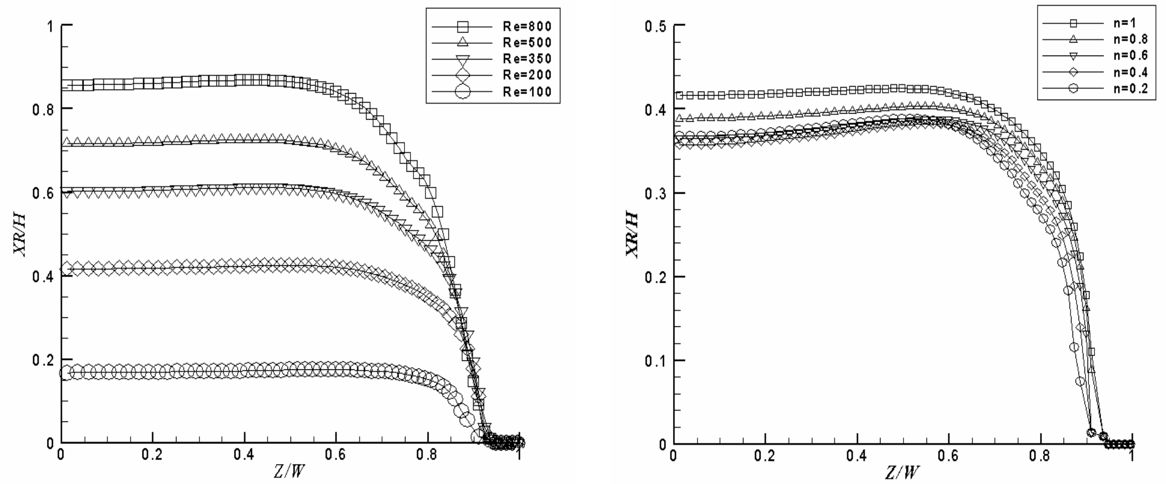

(a) (b)

Fig. 11Recirculation Length (XR) along the spanwise direction; (a)Newtonian fluids (b)Re*=200 versus n.

Shear-thinning is seen to reduce the length of the recirculation everywhere, except in the central region for the smallest value of *n*. The relative variation near the walls is also stronger than in the middle of the cell and shear-thinning also enhances the appearance of the peak value of *XR* at *Z/W*≈ 0.6, thus decreasing the width of the central region of constant *XR* . This complex behavior is further enhanced at higher Reynolds numbers. The recirculation length at the centreplane is plotted in Fig. 12 as a function of Reynolds number and shear-thinning. At Re^* = 800, the behavior is essentially opposite to that found at Re^* = 200 now with the smallest separation belonging to the Newtonian fluid and the longest to the most shear-thinning fluid. The curves pertaining to the different fluids cross each other and explain this behavior. Note that the Kozicki Reynolds number is appropriate for fully-developed duct flow, whereas here we have a complex flow with three-dimensional effects, flow separation, strong changes of direction, and naturally the definition of an apparent viscosity inherent in the Kozicki Reynolds number hardly applies here. Other important conclusions from Fig. 12 are that, the recirculation length increases with increasing Reynolds number regardless of the shear-thinning intensity and that the effect of Reynolds number strengthened with shear-thinning.

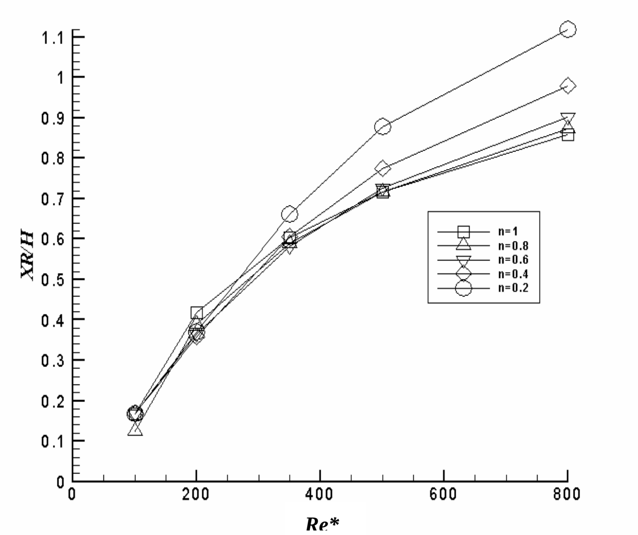

Fig. 12 Recirculation length versus Re* for several power law indexes.

7.3 Three dimensional effects

Three dimensional effects were already apparent in the results of the recirculation length, but are shown here in terms of velocity profiles. These three-dimensional effects are not numerical artifacts and were confirmed experimentally by (Cavadas et al.[2]) using flow visualization techniques.

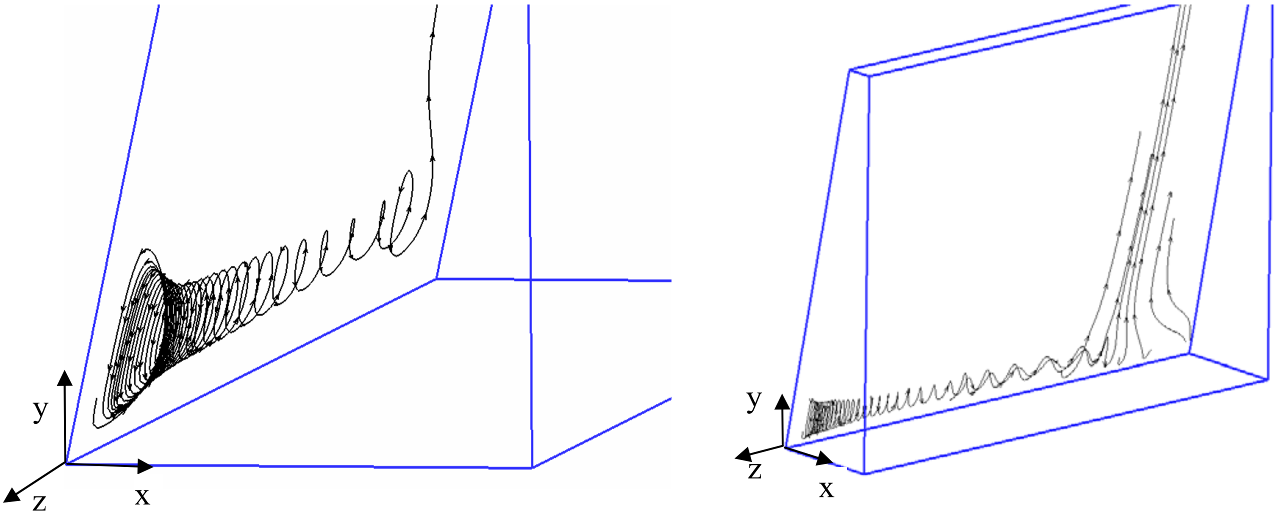

a) b)

Fig. 13 (a) Streamtraces in the recirculation zone; (b) Streamtraces for Re^{*}=200

This behavior can be seen in Fig. 13a) that shows streamlines drawn from the Newtonian numerical predictions at *Re**= 200.

The visualized three-dimensional flow inside the separated flow region was confirmed by the predictions and consists of a helical fluid motion along the spanwise direction from the centre of the cell towards the flat walls, as represented in Fig. 13a). Before reaching the flat side walls, the fluid in helical motion exits the separated flow region and goes into the main flow creating a jet near the side walls. The presence of these near-wall jets were already seen in **Fig.** 5b) at Y/H= 1.65 and X/H=0.525 downstream of the recirculation (c.f. **Fig.** 5a)). Figure Fig. 13b) shows streamlines drawn from the Newtonian numerical predictions at *Re**= 200 and confirms that the predictions were able to capture this effect.

8. CONCLUSIONS

Numerical predictions of the flow of Newtonian and shear-thinning fluids inside a cell, located at the end of a rectangular duct, were carried out using a finite volume based code. The differencing schemes used were all of at least second-order accuracy in uniform grids and the predictions compared well with experimental and analytical data where available. The shear-thinning fluids were modeled by the power law viscosity equation, where the power index varied between 0.2 and 1 and the Kozicki Reynolds number of the approaching rectangular duct flow varied between 100 and 800. The calculations showed the main features of the flow within the cell and quantified in depth the variations of the recirculation length and of the pressure drop coefficient. The use of a simplified 1D theory for the pressure loss, adapted from the theory of Oliveira and Pinho [11] for sudden expansions, allowed an understanding of the causes underlying the pressure loss, as it qualitatively quantified the amount due to frictional loss at walls, the amount due to non-uniformities in pressure and changes in the velocity profiles, as well as the amount due to reversible changes.

The pressure loss coefficient was seen to vary in inverse proportion to the Reynolds number as is typical of flow dominated by viscous effects, in spite of the large Reynolds numbers involved, for all values of n. The largest contribution to the pressure loss coefficient, at all Reynolds numbers, was that accounting for the difference between fully-developed and real wall friction at the inlet and outlet ducts, whereas the contribution associated with distortions of the velocity profiles at inlet and outlet (ΔC_{β}) was seen to be negligible.

In terms of the length of the separated flow region, this was seen to increase with increase regardless of power law index, but the behavior with shear-thinning was strongly non-monotonic: at low Reynolds numbers the largest values of XR pertained to Newtonian fluids, whereas at large Reynolds number the Newtonian fluids had the smallest recirculations.

Three- dimensional effects were found in both the recirculation length and in the velocity profiles, with the numerical predictions being able to capture the features observed by flow visualization.

9. ACKNOWLEDGEMENTS

The authors acknowledge funding by FCT and FEDER via the budget of Centro de Estudos de Fenómenos de Transporte and Projects POCI56342/EQU/2004 and POCI59338/EME/2004 and A.S. Cavadas is greatful to FCT for the PhD grant BD/7091/2001.

10. REFERENCES

[1] Alves, M.A., Oliveira, P.J. and Pinho, F.T., "A convergent and universally bounded interpolation scheme for the treatment of advection", *Int. J. Numer. Meth. Fluids*, Vol. 47, pp 665-679, (2003).

[2] Cavadas, A.S., Campos, J.B.L.M., Pinho, F.T., " Flow field in a liquid impinging jet confined by slopping plane walls", *13th International symposium on applications of laser techniques to fluid mechanics*, session 15.5, separated flows, Lisbon, 26-29 June 2006

[3] Escudier, M.P., Gouldson, I.W., Pereira, A.S., Pinho, F.T., Poole, R.J., "On the reproducibility of the rheology of shear-thinning liquids, *J. Non-Newtonian Fluid Mech.* 97 (2001) 99-124.

[4] Garimella, S.V., and R.A. Rice, "Confined and submerged liquid jet impingement

heat transfer", *ASME J. Heat transfer*,117, 871(1995)

[5] Issa, R.I., Oliveira, P.J., "Numerical predictions of phase separation in two-phase flow through T-junctions", *Comput. Fluids*, 23, 347-372, (1994)

[6] Kozicki, W., Chou, C.H. and Tiu C., "Non-Newtonian flow in ducts of arbitrary cross-sectional shape", *Chem. Eng. Sci.*, Vol. 21, pp 665-679, (1966).

[7] Martin, H., "Heat and mass transfer between impinging gas jets and solid surfaces", *Adv. Heat Transfer*, 13, 1 (1977)

[8] Miranda, João M., Campos, João B.L.M., "Impinging jets confined by a conical wall: laminar flow predictions" *AIChE journal* ,vol. 45, Nº 11 (1999)

[9] Oliveira, P.J., "Compute modeling of multidimensional multiphase flow and application to T-junctions", Ph.D. thesis, Imperial College , London, U.K, (1992).

[10] Oliveira, P.J., Pinho, F.T., Pinto, G.A., "Numerical simulation of non-linear elastic flows with a general collocated finite volume method", *J. Non-Newtonian Fluid Mech.,* 79, 1-43, (1998)

[11] Oliveira, P.J., Pinho, F.T., "Pressure drop coefficient of laminar Newtonian flow in axisymmetric sudden expansions", *Int. J. Heat Fluid Flow*, 18, 518-529, (1997)

[12] Patankar, S.V., "Numerical Heat Transfer and Fluid Flow", Hemisphere Publishing company, Washington, (1980)

[13] Perić, M., "A finite volume method for the prediction of three-dimensional fluid flow in complex duct", Ph.D. thesis, Imperial College , London, U.K, (1985)

[14] White, F.M., "Viscous fluid Flow", 2^{nd} ed. *McGraw-Hill*,(1991)

[15] Van Doormal, J.P., Raithby G.D, "Enhancements of the SIMPLE method for predicting incompressible fluid flows", *Numer. Heat Transfer* 7, 147-163, (1984)